

Pollution resistance of Saturn's ring particles during micrometeoroid impact

Received: 27 October 2023

Accepted: 25 October 2024

Published online: 16 December 2024

 Check for updatesRyuki Hyodo^{1,2,3,4,5}✉, Hidenori Genda² & Gustavo Madeira³

Saturn's rings have been estimated to be as young as about 100 to 400 million years old according to the hypothesis that non-icy micrometeoroid bombardment acts to darken the rings over time and the Cassini observation indicated that the ring particles appear to be relatively clean. These young age estimates assume that the rings formed out of pure water ice particles with a high accretion efficiency of impacting non-icy micrometeoroid material ($\eta \geq 10\%$). Here we show, using numerical simulations of hypervelocity micrometeoroid impacts on a ring particle, that non-icy material may not be as readily accreted as previously thought. We found that the complete vaporization and expansion of non-icy impactor material on energetic collision with a ring particle leads to the formation of charged nanoparticles and ions that are subsequently removed from the rings through collision with Saturn, gravitational escape or electromagnetic drag into Saturn's atmosphere. Despite uncertainties in our models that assume no porosity, strength or ring particle granularity, we suggest minimal accretion of non-icy materials would occur following micrometeoroid impact. This pollution resistance mechanism implies a low accretion efficiency ($\eta \lesssim 1\%$). Thus we suggest that the apparent youth of Saturn's rings could be due to pollution resistance, rather than indicative of young formation age.

The energetic impact of non-icy micrometeoroids on Saturn's rings¹ has been used to estimate the age of the rings^{2–6}. In this study, we use three distinct numerical methods to investigate in detail the sequential processes that occur during micrometeoroid collisions with ring particles (Fig. 1): (1) impact vaporization, (2) condensation within the expanding vapour and (3) electrodynamic interactions of charged nanoparticles and/or ions within Saturn's magnetic and gravitational fields. We demonstrate a pollution resistance mechanism that could contradict the widely held belief that non-icy dark substances of micrometeoroids contribute significantly to ring darkening. Instead, our findings suggest that the impactor's dark material is efficiently removed from the rings; thus it is not as readily incorporated into the rings as previously thought.

Micrometeoroid impact outcomes

A micrometeoroid, composed almost entirely of non-icy material², impacts a particle in Saturn's ring typically at velocities approximating

$v_{\text{imp}} \approx 30 \text{ km s}^{-1}$ (Fig. 1). We performed three-dimensional (3D) smoothed particle hydrodynamics (SPH) impact simulations (Fig. 2 and Methods). We assume a non-porous and strengthless impactor and an infinite target of idealized by H_2O ice or SiO_2 composition, and that the impactor is much smaller than the ring particle but much larger than individual ring-particle regolith grains. The presence of porous and regolith structures, as well as the wide variation in particle sizes, could lead to diverse outcomes on impact. The relevant equation of state (EOS) for water ice was a five-phase EOS⁷. That for non-ice materials, denoted by silicate, was idealized by the SiO_2 M-ANEOS EOS⁸.

Our impact simulations showed that such a high-speed impact event leads to a vaporization of the whole impactor's material with a peak temperature of $\geq 10,000 \text{ K}$ and a peak pressure of $\geq 100 \text{ GPa}$ for both H_2O ice and non-icy (here quartz, SiO_2) materials (Fig. 3, Methods and Supplementary Information). Hence, no exogenic material is directly implanted in the rings in solid form. As the impact shock

¹ISAS/JAXA, Sagami-hara, Japan. ²Earth-Life Science Institute, Institute of Science Tokyo, Tokyo, Japan. ³Université Paris Cité, Institut de Physique du Globe de Paris, CNRS, Paris, France. ⁴Galaxies Inc., Tokyo, Japan. ⁵SpaceData Inc., Tokyo, Japan. ✉e-mail: hyodo@elsi.jp

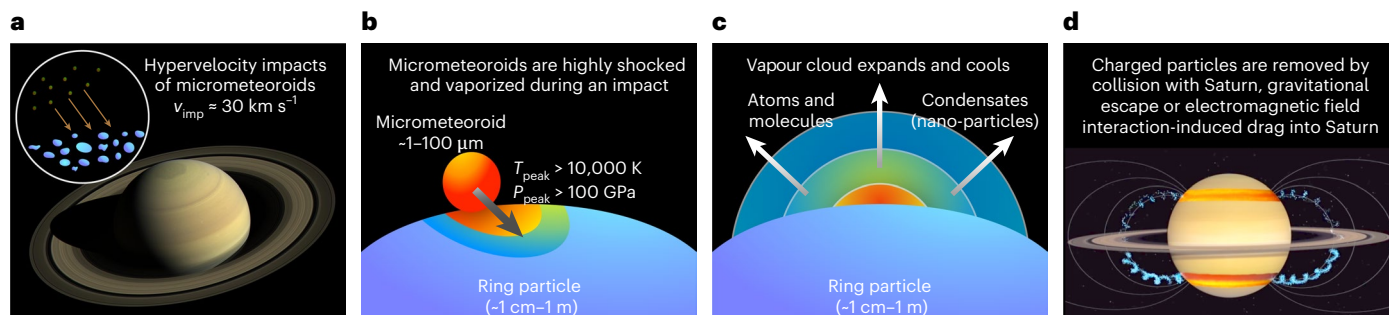


Fig. 1 | Pollution resistance mechanism for Saturn's ring particles.

a, Micrometeoroid impacts on Saturn's rings occur at impact velocities of $\sim 30 \text{ km s}^{-1}$. **b**, The impactor materials are highly shocked ($>100 \text{ GPa}$) and form hot expanding vapour ($>10,000 \text{ K}$). Only a small fraction of the ring particles (mass comparable to the impactor) is vaporized. **c**, The impact-generated vapour expands with a high velocity (on average $>14 \text{ km s}^{-1}$), producing atoms/molecules and forming

nanoparticles as condensates. The silicate vapour is more prone to condensation than water vapour. **d**, Atoms or molecules are ionized and nanoparticles are charged in Saturn's magnetosphere, and impactor materials are removed from the ring plane by direct collision with Saturn, by escape from Saturn's gravitational field or by being dragged into Saturn by interaction with the electromagnetic field. Credit: **d**, NASA Goddard Space Flight Center.

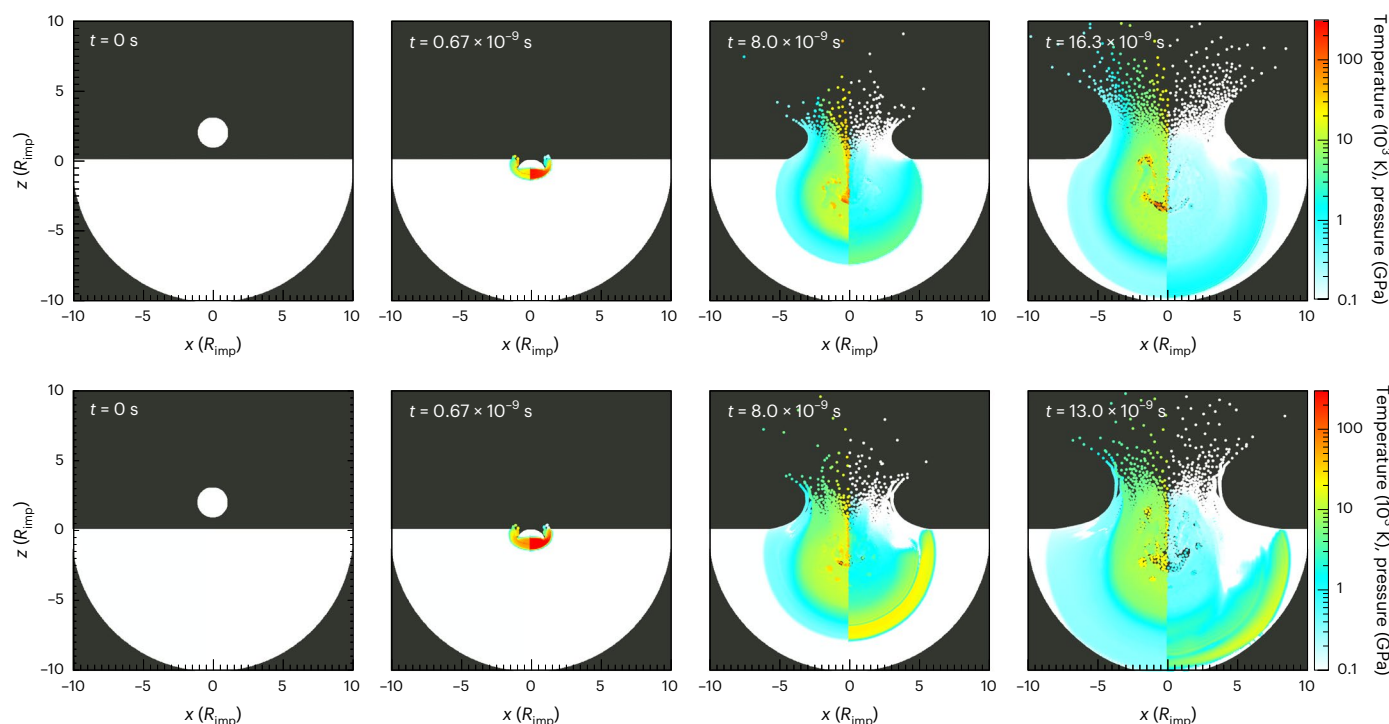


Fig. 2 | Time evolution of our SPH impact simulation ($v_{\text{imp}} = 30 \text{ km s}^{-1}$). Impacts occur in the x - z plane in the $-z$ direction (vertical impact). Cross sections (particles within $y = \pm 0.1 R_{\text{imp}}$) are plotted. The top and bottom panels show cases of the H_2O ice EOS and the SiO_2 rock EOS, respectively. The left and

right halves of each panel show the temperature and pressure using the colour contour. Plotted time is the case where the impactor radius is $r_{\text{imp}} = 10 \mu\text{m}$, and it is linearly scaled by r_{imp} .

decreases rapidly with the cube of the distance from the impact point⁹, the vapour production of the target material (here the ring particle; water ice) is localized only near the impact point, with a mass comparable to that of the impactor (here the micrometeoroid) (Fig. 2 and Supplementary Information). Non-vaporized particulate ejecta of target materials (ring particles) is launched farther from the impact point with smaller ejection velocity⁹, and its total mass is much larger than the mass of the projectile^{10,11} (Supplementary Fig. 1 and Methods). Such H_2O particulate ejecta originated from ring particles redistributes within the rings and may serve as the source of ballistic transport^{3,4,12}.

Fate of the impact vapour

We then study the fate of the impact vapour and address the question of recondensation and possible reaccretion by the rings. The impact

vapour expands and cools adiabatically¹³. We performed simulations of condensate formation within an expanding vapour¹⁴, using either H_2O for five-phase EOS⁷ or SiO_2 for M-ANEOS EOS⁸ (Methods); that is, we assume no mixing between the impactor and the target material. Altering the EOS would lead to changes in the condensation chemistry, affecting variables such as the two-phase boundary conditions, latent heat and surface tension. The detailed chemical network involved in the condensation process is outside the scope of our study.

In Fig. 4a, we show the pressure and temperature evolution of the silicate vapour that originates from the impactor (initial temperature of $\geq 60,000 \text{ K}$ and pressure of $\geq 1,000 \text{ GPa}$; Fig. 3). The expanding silicate vapour reaches the liquid/vapour two-phase boundary, resulting in the supercooled state, and nucleation occurs (formation of condensates). As latent heat is released through nucleation, the supercooled state is

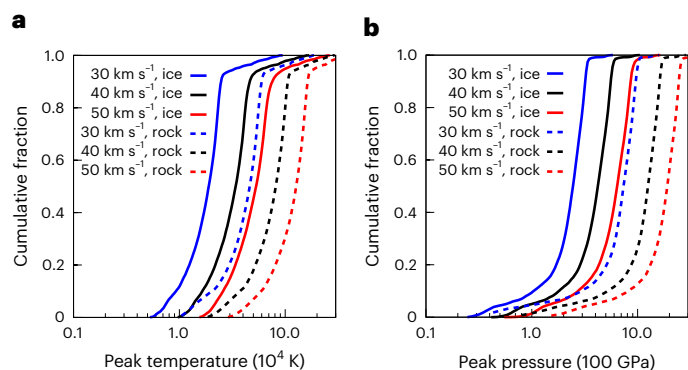


Fig. 3 | Cumulative distribution of the peak temperature and peak pressure that our modelled impactor experiences. a, Peak temperature. b, Peak pressure (see also Supplementary Fig. 1). Solid and dashed lines represent cases of the H₂O ice EOS and the SiO₂ rock EOS, respectively, for different impact velocities. Here target material is not included because the impactor's materials, potential ring darkening material, are the focus of this study.

forced back to the two-phase curve and the vapour continues to expand along the near two-phase curve. During this phase, the existing condensates grow through collisions with remaining vapour molecules. The system finally reaches quenching when the vapour becomes too sparse to collide with the condensates. This evolution is the scale invariance for the impact size (Methods).

Cassini results indicate that the size of the micrometeoroids is $r_{\text{imp}} \approx 1\text{--}100\ \mu\text{m}$ and that larger micrometeoroids contribute more to the total impacting mass of the rings². Our condensation simulations show that the size of the condensates is in the range of 10^{-10} to $10^{-9}\ \text{m}$, and $\sim 60\%$ of the impact vapour does not condense, persisting as neutrals and/or ions for $v_{\text{imp}} \approx 30\ \text{km s}^{-1}$ (Supplementary Information)¹⁴. A slower impact velocity, that is, a lower entropy case, produces larger condensates (Supplementary Fig. 2). This suggests that a combination of the low-velocity collision (for example, $<30\ \text{km s}^{-1}$) and a large impactor (for example, $\geq 10\ \mu\text{m}$) can produce the observed nano-sized particles¹⁵.

Water vapour is also produced. The expansion of the water vapour follows a different evolution from that of the silicate vapour (Fig. 4b). Regardless of the size of the impactor, we found that the water vapour hardly condenses during the expansion. The critical point of the water vapour is at a lower temperature T , pressure P and density ρ than those of the silicate vapour in the T – P phase and $1/\rho$ – T phase. The adiabatic evolution paths of water vapour starting from our initial T , P and ρ conditions ($\geq 10,000\ \text{K}$ and $\geq 100\ \text{GPa}$; Fig. 3) always intersect with the two-phase boundary at very low densities ($\rho \ll 10^{-5}\ \text{kg m}^{-3}$). The water vapour scarcely becomes dense enough to form a condensate, remaining predominantly as neutrals and/or ions throughout the expansion phase.

Interaction between charged particles and the magnetosphere

Condensates and the remnant vapour would expand from the impact point^{11,16}. Within the plasma environment of Saturn's magnetosphere,

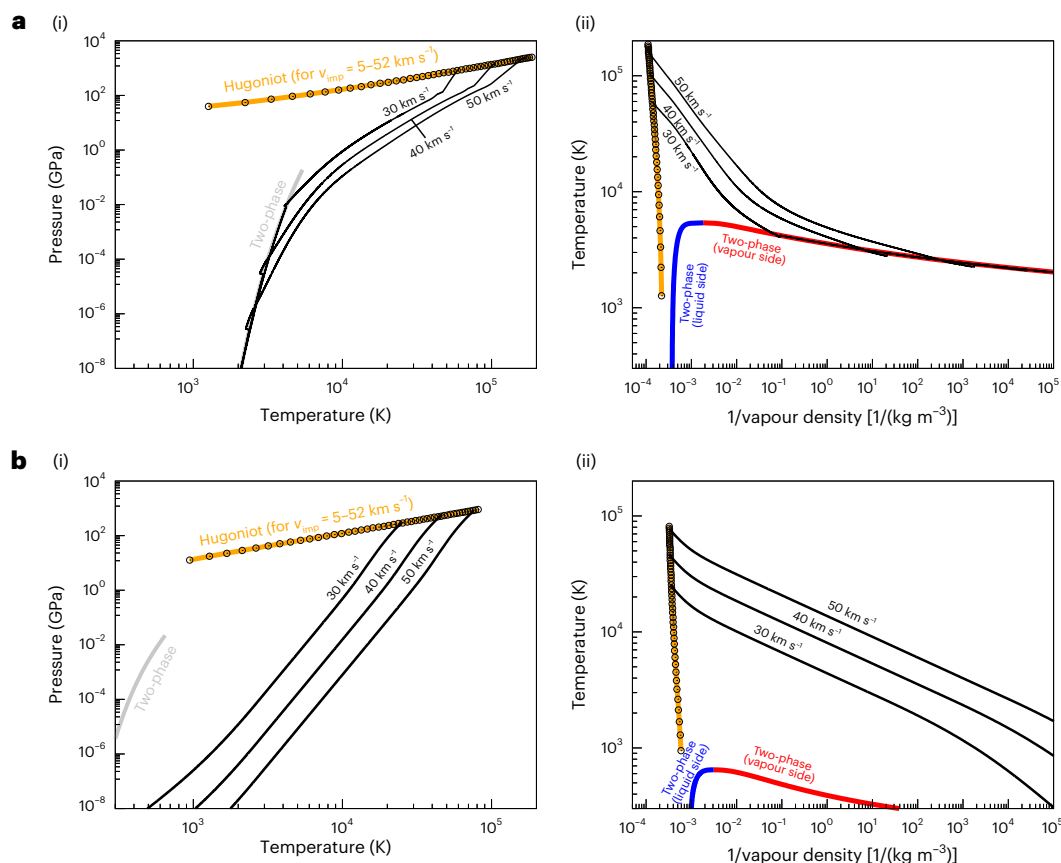


Fig. 4 | Numerical results of vapour expansion and condensation processes. a, Silicate vapour expansion (SiO₂ ANEOS EOS): (i) T – P evolution; (ii) $1/\rho_{\text{vap}}$ – T evolution. Black lines correspond to cases of $v_{\text{imp}} = 30, 40$ and $50\ \text{km s}^{-1}$ cases, as marked. The initial conditions are obtained from the impact simulations. **b, The same as a but for the case of water vapour (five-phase H₂O EOS).** In all cases of water vapour, because the vapour density is too low when the system reaches

the two-phase boundary, viable nucleation hardly occurs, remaining as neutral/ionized atoms and/or molecules. The grey lines in **a** (i) and **b** (i) indicate the two-phase boundary. The blue and red lines in **a** (ii) and **b** (ii) indicate the two-phase boundaries that separate the liquid and vapour regions from the liquid–vapour region, respectively (the vapour dome). The Hugoniot curve for $v_{\text{imp}} = 5\text{--}52\ \text{km s}^{-1}$ is displayed with orange lines, and open circles are plotted at intervals of $1\ \text{km s}^{-1}$.

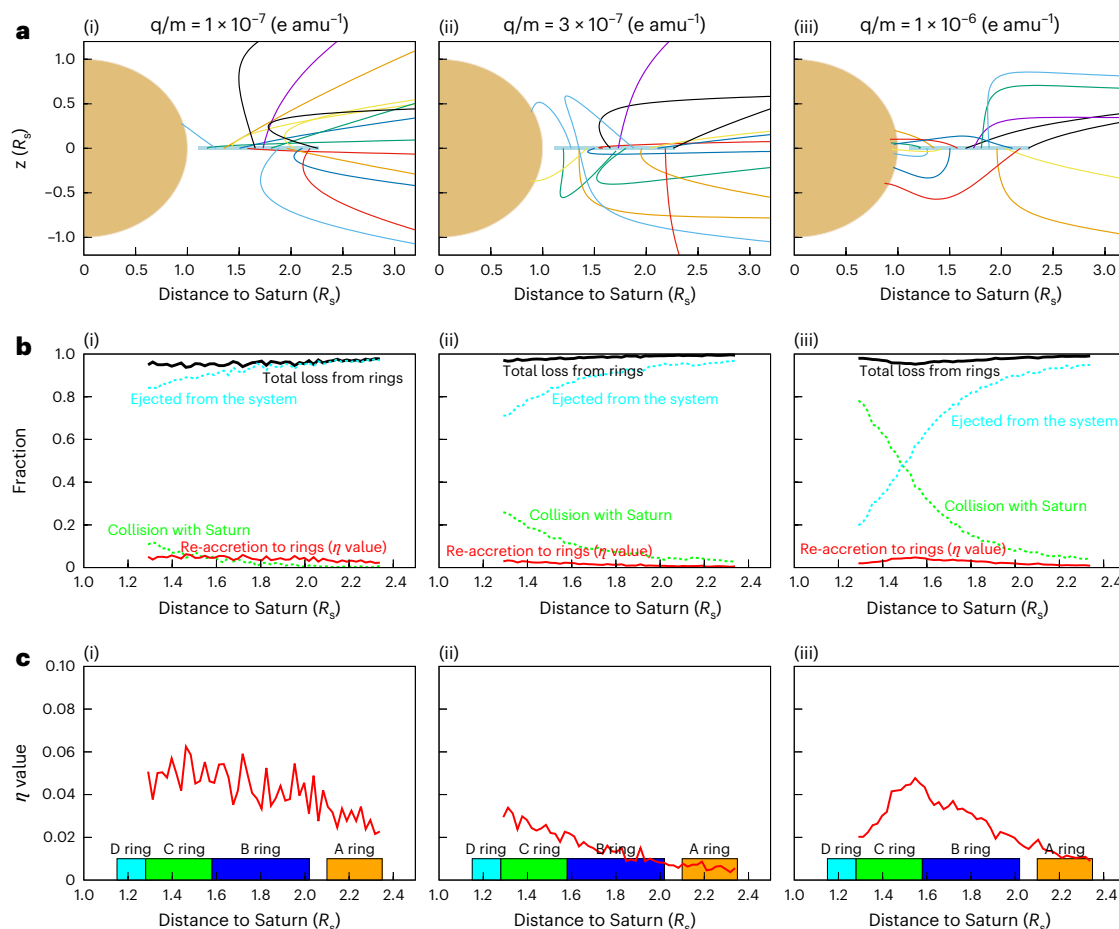


Fig. 5 | Numerical results of the dynamical evolution of charged particles for different q/m ratios. **a**, Fifteen randomly selected particle trajectories out of a total of 10^5 trajectories. **b**, The fraction of particles with different fates: collision with Saturn (green lines), ejection from the system (cyan lines), re-collision with

rings (red lines; corresponds to the accretion efficiency of impactor's material, η value) and total removal from the rings (collision with Saturn or ejection from the system; black lines). **c**, Close-up of **b** (only the η value is shown; red lines).

neutrals and nanoparticles are ionized^{15,17–19}. We have conducted additional simulations to analyse the dynamical evolution of these charged nanoparticles and ions, which includes interactions with Saturn's gravitational and electromagnetic fields (Methods and Fig. 5). The interplay between dust, plasma and the magnetosphere allows these charged nanoparticles and ions, which originate from Saturn's main rings, to be dragged into both hemispheres of Saturn's atmosphere^{15,18,20}. These particles could also be the source of nanometre-sized particles that are ejected from the Saturnian system, referred to as stream particles^{15,19,21}. Our dynamical simulations demonstrate that the accretion efficiency of the impactor's material to the rings η could be remarkably low—only around $\eta \approx 1$ –3% (Fig. 5). The charge-to-mass ratio q/m is a critical parameter that governs the accretion efficiency. A higher q/m results in more efficient coupling with the magnetic field, leading to less efficient ejection from the system but more efficient collision with Saturn.

We note that our estimates of η are based on the form of the charged nano-sized condensates and ions/molecules produced by the high-energy impacts, which are completely different from the original materials of the impactors. However, these altered impactor materials may not always have the non-icy properties assumed and detectable by Cassini's microwave radiometry observations^{5,6}. Therefore, our η value could be considered as an upper limit. In addition, it is important to note that the point of deposition is not identical to the point where the micrometeoroid strikes the rings.

The series of events delineated in the preceding—the generation and expansion of impact vapour, followed by condensation and

ionization and, ultimately, expulsion from Saturn's rings through direct removal and electromagnetic field interactions—suggest an inefficient darkening of Saturn's ring particles by exogenic non-icy materials. This inference arises from the fact that the impact process itself effectively cleans the material of the incoming impactor within the Saturn system. We refer to this as an effective pollution resistance mechanism, which could fundamentally redefine our understanding of the age of Saturn's rings. Previous studies estimating the rings' age to be approximately 100–400 Myr assumed a somewhat efficient accretion of impactor material (with $\eta \geq 10\%$ efficiency) and a constant mass flux from micrometeoroid bombardment^{2–4}. However, the accretion efficiency of as small as $\eta \lesssim 1\%$ (Fig. 5) suggested by our study may imply that the rings' maximum age could extend into billions of years.

The hypervelocity micrometeoroid impacts may be the causes of the ring rain^{15,20,22} and streaming particles^{17,21}, and an enigmatic higher non-icy fraction in nanoparticles outside the main rings (up to ~30%) than within the main rings (typically on the order of ~1% by mass) has been reported¹⁵. Although there are large uncertainties in the observed mass flux of the ring rain²³, assuming a simple linear correlation with the meteoroid flux, our estimate of the minimum vapour mass production rate ($\sim 716.2 \text{ kg s}^{-1}$), that is the minimum total production rate of ions and nanoparticles using the updated meteoroid flux², is in the range of the ring rain observations (~ 432 – $2,870 \text{ kg s}^{-1}$) (refs. 23–25) (Supplementary Information).

Our findings indicate that only a minor fraction of a ring particle, specifically around the impact point, undergoes vaporization. This

vapour volume from the target is roughly equivalent to the volume of the impactor, with the target composition being nearly 100% water^{5,6}. Conversely, the impactor is entirely vaporized, with its composition being approximately 100% non-icy². These findings suggest a natural explanation for the high abundance of non-icy materials reported outside the main rings¹⁵, proposing that they could originate from the energetic impact process (Supplementary Information).

Implications for the age of Saturn's rings and beyond

Assuming a linear dependence of age on η , our results of $\eta \lesssim 1\%$ suggest that Saturn's rings could be as old as the age of the solar system, even though they look clean and young based on today's low non-icy content²⁶. Our numerical simulations indicated that the exogenic non-icy dark materials from the incoming micrometeoroid impactor are not efficiently incorporated into the rings. Instead, they are likely to be removed from the rings and could escape Saturn's gravitational field or be absorbed by Saturn's atmosphere. Therefore, the concept of exposure age, which suggests that Saturn's rings are young based on the cumulative accumulation of dark micrometeoroid material, should not be solely relied on to conclusively estimate the age of the rings.

On another note, the ballistic transport model offers a separate line of theoretical dynamical reasoning. This model, independent of micrometeoroid-induced darkening, could support the idea of the rings' relative youth^{3,4,12}. The ballistic transport model provides explanations for several ring structure characteristics, such as the contrast in darkening between the C ring and A and B rings^{3,4}. However, the structure age can differ from the real age, and these results significantly depend on the impact yield parameter, which is currently poorly defined²⁶.

This work would motivate the community to pursue further research in areas such as the effects of particle porosity, granularity and/or condensation chemistry. The inclusion and mixing of various materials, such as metals and organics, can modify the thermodynamic pathways relevant to impact and condensation processes, as well as affect the subsequent charging processes. For example, the incorporation of iron might result in the formation of larger iron condensates due to a higher surface tension and a higher condensation temperature at a higher vapour density compared with silicate. Alternatively, when iron is oxidized, its surface tension is comparable to that of silicate²⁷, and the result could be similar to that studied here. We conducted separate analyses on the behaviour of H₂O and SiO₂ vapours, chosen to represent low and high impedance cases, respectively. The thermodynamic behaviour of a mixed vapour containing both H₂O and SiO₂ may fall between the characteristics observed in the pure H₂O and pure SiO₂ cases. These unexplored complicated scenarios offer valuable questions for future studies.

However, it is important to note that irrespective of the material properties, the resultant condensates are expected to be considerably smaller than the micrometeoroid impactor²⁸. This is because the condensates form from the expanding vapour, and the initial volume of vapour is not substantially larger than that of the impacted micrometeoroid (Supplementary Fig. 3). These small condensates ($\ll 1\text{--}100\ \mu\text{m}$) typically become charged within the Saturn system, increasing the likelihood of their ejection from the rings^{17,18}.

Finally, high-velocity impacts leading to the creation of charged nanoparticles and ions could potentially occur in places such as the Uranian and Neptunian rings and icy moons around giant planets. While this mechanism may not alter the bulk composition of the impacted target, it suggests that surface composition could change. In addition, new material from impactors may not be efficiently incorporated into the rings or surfaces of moons, but instead transported elsewhere. Therefore, the bulk compositional differences observed in various ring systems among the giant planets could be attributed to their formation processes, for example, when building

material comes from the outside of the system²⁹, rather than to post-formation dynamics.

Online content

Any methods, additional references, Nature Portfolio reporting summaries, source data, extended data, supplementary information, acknowledgements, peer review information; details of author contributions and competing interests; and statements of data and code availability are available at <https://doi.org/10.1038/s41561-024-01598-9>.

References

- Chambers, L. S., Cuzzi, J. N., Asphaug, E., Colwell, J. & Sugita, S. Hydrodynamical and radiative transfer modeling of meteoroid impacts into Saturn's rings. *Icarus* **194**, 623–635 (2008).
- Kempf, S. et al. Micrometeoroid infall onto Saturn's rings constrains their age to no more than a few hundred million years. *Sci. Adv.* **9**, eadf8537 (2023).
- Durisen, R. H. & Estrada, P. R. Large mass inflow rates in Saturn's rings due to ballistic transport and mass loading. *Icarus* **400**, 115221 (2023).
- Estrada, P. R. & Durisen, R. H. Constraints on the initial mass, age and lifetime of Saturn's rings from viscous evolutions that include pollution and transport due to micrometeoroid bombardment. *Icarus* **400**, 115296 (2023).
- Zhang, Z. et al. Exposure age of Saturn's A and B rings, and the Cassini Division as suggested by their non-icy material content. *Icarus* **294**, 14–42 (2017).
- Zhang, Z. et al. Cassini microwave observations provide clues to the origin of Saturn's C ring. *Icarus* **281**, 297–321 (2017).
- Senft, L. E. & Stewart, S. T. Impact crater formation in icy layered terrains on Mars. *Meteorit. Planet. Sci.* **43**, 1993–2013 (2008).
- Melosh, H. J. A hydrocode equation of state for SiO₂. *Meteorit. Planet. Sci.* **42**, 2079–2098 (2007).
- Hyodo, R. & Genda, H. Escape and accretion by cratering impacts: formulation of scaling relations for high-speed ejecta. *Astrophys. J.* **898**, 30 (2020).
- Hyodo, R. & Genda, H. Erosion and accretion by cratering impacts on rocky and icy bodies. *Astrophys. J.* **913**, 77 (2021).
- Melosh, H. J. *Impact Cratering: A Geologic Process* (SAO/NASA Astrophysics Data System, 1989).
- Cuzzi, J. N. & Durisen, R. H. Bombardment of planetary rings by meteoroids: general formulation and effects of Oort cloud projectiles. *Icarus* **84**, 467–501 (1990).
- Raizer, Y. P. Condensation of a cloud of vaporized matter expanding in vacuum. *Sov. Phys. JETP* **10**, 1229–1235 (1960).
- Johnson, B. C. & Melosh, H. J. Formation of spherules in impact produced vapor plumes. *Icarus* **217**, 416–430 (2012).
- Hsu, H.-W. et al. In situ collection of dust grains falling from Saturn's rings into its atmosphere. *Science* **362**, eaat3185 (2018).
- Wilson, G. R. & Waite Jr, J. H. Kinetic modeling of the Saturn ring-ionosphere plasma environment. *J. Geophys. Res. Space Phys.* **94**, 17287–17298 (1989).
- Hsu, H.-W. et al. Stream particles as the probe of the dust-plasma-magnetosphere interaction at Saturn. *J. Geophys. Res. Space Phys.* **116**, A09215 (2011).
- Mace, M. J. T., Birkinshaw, M. & Leinhardt, Z. M. A chance of rain: investigating the effects of stochastic charging on the orbital dynamics and precipitation of nanodust in Saturn's rings. *Mon. Not. R. Astron. Soc.* **522**, 4862–4874 (2023).
- Horányi, M., Morfill, G. & Grün, E. Mechanism for the acceleration and ejection of dust grains from Jupiter's magnetosphere. *Nature* **363**, 144–146 (1993).
- Ip, W.-H., Liu, C.-M. & Pan, K.-C. Transport and electrodynamical coupling of nano-grains ejected from the Saturnian rings and their possible ionospheric signatures. *Icarus* **276**, 163–169 (2016).

21. Kempf, S. et al. High-velocity streams of dust originating from Saturn. *Nature* **433**, 289–291 (2005).
22. Northrop, T. G. & Connerney, J. E. P. A micrometeorite erosion model and the age of Saturn's rings. *Icarus* **70**, 124–137 (1987).
23. O'Donoghue, J. et al. Observations of the chemical and thermal response of 'ring rain' on Saturn's ionosphere. *Icarus* **322**, 251–260 (2019).
24. O'Donoghue, J. et al. The domination of Saturn's low-latitude ionosphere by ring 'rain'. *Nature* **496**, 193–195 (2013).
25. Moore, L., O'Donoghue, J., Müller-Wodarg, I., Galand, M. & Mendillo, M. Saturn ring rain: model estimates of water influx into Saturn's atmosphere. *Icarus* **245**, 355–366 (2015).
26. Crida, A., Charnoz, S., Hsu, H.-W. & Dones, L. Are Saturn's rings actually young?. *Nat. Astron.* **3**, 967–970 (2019).
27. Kozasa, T. & Hasegawa, H. Formation of iron-bearing materials in a cooling gas of solar composition. *Icarus* **73**, 180–190 (1988).
28. O'Keefe, J. D. & Ahrens, T. J. Impact and explosion crater ejecta, fragment size, and velocity. *Icarus* **62**, 328–338 (1985).
29. Hyodo, R., Charnoz, S., ébastien, Ohtsuki, K. & Genda, H. Ring formation around giant planets by tidal disruption of a single passing large Kuiper belt object. *Icarus* **282**, 195–213 (2017).

Publisher's note Springer Nature remains neutral with regard to jurisdictional claims in published maps and institutional affiliations.

Open Access This article is licensed under a Creative Commons Attribution-NonCommercial-NoDerivatives 4.0 International License, which permits any non-commercial use, sharing, distribution and reproduction in any medium or format, as long as you give appropriate credit to the original author(s) and the source, provide a link to the Creative Commons licence, and indicate if you modified the licensed material. You do not have permission under this licence to share adapted material derived from this article or parts of it. The images or other third party material in this article are included in the article's Creative Commons licence, unless indicated otherwise in a credit line to the material. If material is not included in the article's Creative Commons licence and your intended use is not permitted by statutory regulation or exceeds the permitted use, you will need to obtain permission directly from the copyright holder. To view a copy of this licence, visit <http://creativecommons.org/licenses/by-nc-nd/4.0/>.

© The Author(s) 2024

Methods

Impact simulation

We performed 3D SPH impact simulations to study the hypervelocity micrometeoroid impacts on a ring particle. We used the standard SPH method³⁰. For the artificial viscosity, we used a Von Neumann–Richtmyer-type viscosity with typical parameters of $\alpha = 1.0$ and $\beta = 2.0$. We confirmed that using different viscosities (for example, $\alpha = 2.0$ and $\beta = 4.0$) does not affect the resultant distribution of peak pressure and peak temperature. The Mach number for the 30 km s⁻¹ impacts is about 10 for both silicate and ice. Our code has adapted a variable time step that fully satisfies the Courant–Friedrichs–Lewy condition and depends on the strength of the shock wave, so that the time step becomes smaller as the shock propagates. The artificial viscosity is also varied as a function of Mach number³¹. For the kernel function, we used the spherically symmetric spline kernel function proposed by ref. 32.

Our numerical code was the same as that used in previous studies^{9,10,33,34}. The ejection behaviour seen in our SPH simulations was compared with and reproduced by the recent impact experiments³⁵. The post-impact thermodynamic conditions (such as temperature T and pressure P) were investigated. These data are used as initial conditions for condensation simulations. The relevant EOS for water ice was a five-phase EOS⁷. That for non-ice materials, denoted by silicate in our study, was idealized by the quartz, SiO₂, M-ANOE EOS⁸, as the thermodynamic data for quartz have been extensively studied and the data are sufficiently large and reliable. For simplicity, the same EOS was used for both the impactor and the target.

Since a ring particle (–1 cm–1 m; here target) is much larger than the typical micrometeoroid (–1–100 μ m; ref. 2), the target was idealized as a hemisphere with a flat surface on the impact side. For numerical resolution, the total number of equal mass SPH particles (for target and impactor) used in our simulations was $\sim 1.7 \times 10^7$. The diameter of the impactor is resolved by 20 SPH particles, and the total number of SPH particles in the impactor is 33,510. The target is ten times larger than the impactor. The impactor and target are created by distributing the SPH particles in a 3D lattice (face-centred cubic).

In the real Saturn's system, the target (ring particle) is significantly larger than the impactor (micrometeoroid). However, due to computational constraints, we set the target's radius to be ten times that of the impactor's. This numerical limitation does not affect our study's primary focus, the vapour mass and impactor material, since vapour formation occurs predominantly near the impact point, and we confirmed that our simulations are long enough to converge the peak pressure and temperature recorded by the impactor's material. We stopped our simulations just before the shock wave reached the target boundary and analysed the data there.

The impact velocity was 30, 40 or 50 km s⁻¹, and head-on impact was assumed. During the impact process, each SPH particle experienced a different temperature/pressure evolution. We tracked each time step within the simulation, recording the peak temperature and peak pressure experienced by each particle until the end of the simulation (see also Supplementary Fig. 1).

For the condensation simulations, we used the values at ~90% of the cumulative distribution shown in Fig. 3. For the case of silicate, these are (T, P) = (6.07×10^4 K, 961 GPa), (1.06×10^5 K, 1,610 GPa) and (1.64×10^5 K, 2,450 GPa) for 30 km s⁻¹, 40 km s⁻¹ and 50 km s⁻¹, respectively. For the case of H₂O ice, (T, P) = (2.52×10^4 K, 327 GPa), (4.67×10^4 K, 561 GPa) and (7.60×10^4 K, 879 GPa) for 30 km s⁻¹, 40 km s⁻¹ and 50 km s⁻¹, respectively. These numerical results are in agreement with those estimated by analytical estimates (Supplementary Information).

Note that the 90% cumulative values were our somewhat arbitrary choice as we observed that the width of the distribution was narrow and had the steep slope (Fig. 3). The 90% is not the most likely value, although the definition of the most likely value may need further discussion. In any case, if we choose the 50% cumulative values, the starting points shift slightly to the left (less than a factor of 2). With these new

starting points, the crossing with the two-phase curve occurs at a higher T – P point (that is, at a higher ρ_{vap}), which creates a larger condensate (we can understand this trend by looking at the right panel of Supplementary Fig. 2 for different v_{imp} cases). However, this would not change the resulting size by more than an order of magnitude, and thus we still form nano-sized condensates for the SiO₂ EOS case. In the case of the H₂O ice EOS, such a shift does not change the conclusion, as the crossing occurs at an extremely low density, where condensation is unlikely to occur.

We also compared our results with a previous study of impacts between a ring particle and micrometeoroid¹. First and foremost, it is essential to note the fundamental differences between the 2D CTH and 3D SPH simulation methods. The 2D CTH method is a two-dimensional, mesh-based hydrodynamics approach, whereas the 3D SPH simulation is a particle-based method in three dimensions. Both methodologies have been widely applied in various aspects of impact phenomena within planetary science, including studies on lunar-forming impacts (for example, ref. 36) and crater-forming impacts (for example, ref. 37). Our study does not posit the SPH method as superior to the CTH method; future studies are required for a detailed comparison using the same model settings.

There are notable differences in the impact scenarios between our study and that of ref. 1. Specifically, they used an impactor and target of identical sizes, whereas our simulation assumes a target that is substantially larger, being ten times the size of the impactor. In addition, EOS used in our study differs; we employed the five-phase EOS⁷, which encompasses ice Ih, ice VI, ice VII, liquid and vapour, as well as quartz, SiO₂, M-ANOE EOS⁸. By contrast, Fig. 1 utilized ANEOS pure H₂O ice³⁸ and the ANEOS serpentinite. Regarding the H₂O EOS, ours is an extension of the water state equation that is also used in the industrial field³⁹, and thus we consider ours to be state of the art, particularly in the modelling of H₂O.

In addition to the aforementioned differences, the computational requirements of running 3D SPH simulations are notably high, rendering a direct one-to-one comparison impractical. However, from the perspective of impact physics, as outlined by ref. 11, it is anticipated that the impact point's vicinity would exhibit similar behaviours under comparable conditions of impact velocity, geometry and similar material. We confirmed a good agreement between these techniques. For example, for a 50 km s⁻¹ impact, ref. 1 reported the peak temperature of ~99,000 K and the peak pressure of $\sim 1.3 \times 10^{13}$ dynes cm⁻². Our SPH simulations showed that the peak temperature and peak pressure at ~90% of the cumulative distribution (shown in Fig. 3) are ~76,000 K and ~879 GPa ($\sim 0.879 \times 10^{13}$ dynes cm⁻²), respectively. Therefore, the results obtained from the two different approaches show only a small difference, and such a difference does not change our conclusion.

It is worth mentioning about the dependence on the size. If the impactor and target are strengthless (no friction and no material strength) and have no porosity, all hydrodynamic equations can be rewritten in a dimensionless form¹¹, so that the collisional behaviour does not change by the size. However, Saturn's ring particles are approximately 90% porous⁵. In this case, the size and porosity are important parameters to regulate the outcome of impacts.

Taking into account the target porosity (but using a non-porous impactor) leads to greater vaporization of H₂O ice impacted³⁷. This is because the critical pressure required to vaporize H₂O ice is lower due to the additional PdV work done in compacting the pore space, and the shock wave energy is deposited as thermal energy. However, if the impactor is also porous, there is no guarantee that vapour production will increase. We leave this complex investigation to future studies.

Regarding the track morphology and penetration processes on a porous target, the particle size is an important parameter. The size distribution of regolith particles spans a broad range, from approximately 1 μ m to 10 cm (ref. 40). The size of the impactor, or micrometeoroid, typically ranges from about 1 to 100 μ m (ref. 2). If the impactor size is greater than or equal to the size of the regolith particles, the impactor can penetrate the porous target. According to fig. 4 in ref. 41, significant

penetration (maximum width/penetration depth $< 10^{-1}$) occurs when (dynamic pressure)/(projectile tensile strength) is less than 10. If we consider the reasonable values studied here (target density 100 kg m^{-3} , corresponding to H_2O ice with 90% macroporosity, impact velocity 30 km s^{-1} and projectile tensile strength 20 MPa for basalt), this ratio becomes 4,500. This means that the impact does not result in significant penetration, but in a normal crater. If the size of the impactor is smaller than the size of the regolith particles, the impactor may collide with the monomer of a ring particle. If the monomer is pure H_2O ice (no microporosity), the situation may be similar to our simulation case or ref. 1. This scenario represents an impact where porosity does not play a major role. However, we note that, in this case, infinite mass medium for the target is not reasonable, although the peak shock temperature and pressure near the contact point would not change¹¹.

The porous, granular nature of a regolith layer can be analogized to a 'ball pit' extending to a significant depth. Within this layer, the fate of an impactor can range from head-on to grazing impacts, leading to a variety of outcomes. However, modelling these structures exceeds the capabilities of today's computational models.

Condensation simulation

We performed 1D condensation simulations (Lagrangian approach) of the expansion of an impact vapour cloud into a vacuum to study the typical size of the condensates and the condensation fraction within the vapour. Our approaches were similar to those in ref. 14 and qualitatively reproduced similar results, although the EOS used is not exactly the same, so a direct exact comparison cannot be made (B. C. Johnson, personal communication¹⁴). The evolution includes several steps: nucleation, growth and quenching.

The vapour cloud expands and cools. When the system is supercooled, nucleation is solved; that is, vapour molecules aggregate to form nuclei (at a rate described by equation (3))^{13,42}. The minimum size of the initial nuclei is r_{cri} (equation (1)). The nucleation rate (equation (3)) has an exponential dependence on the degree of supercooling (θ ; equation (2)) and thus almost all nucleation takes place around the maximum supercooling state θ_{max} ; therefore, we can set the artificial minimum θ_{min} above which nucleation has been solved numerically ($\theta_{\text{min}} \approx 0.01$). This procedure stabilizes and saves computational time without changing the results as long as $\theta_{\text{max}} > \theta_{\text{min}}$. During condensation, the latent heat is released and the supercooled state is eventually forced back to the two-phase boundary.

Even after nucleation has stopped, the condensates continue to grow by the balance between absorption of the remaining vapour molecules by collisions (condensation) and evaporation from the nuclei. The growth phase and size evolution were solved numerically by equations (7)–(11). As the existing nuclei grow, the latent heat is released and the system almost follows the two-phase boundary.

The system continues to expand. When the vapour becomes too sparse for the remaining vapour molecules to hit the condensates, the system reaches quenching. The latent heat is then no longer released and the system continues to expand, leaving the two-phase boundary. Here we considered a steady-state approximation where the time to nucleation should be much smaller than the timescale on which the thermodynamic variables change (see more details in B.3. in ref. 14). This prevents further nucleation during quenching and the size of the condensates and the condensation fraction in the vapour (calculated by equation (6)) no longer change.

Models of nucleation and growth. The critical radius r_{cri} below which vaporization takes place (the minimum size of nuclei) is given as

$$r_{\text{cri}} = \frac{2\sigma}{n_{\text{liq}} U_{\text{eva}} \mu \theta} = \frac{2\sigma}{\rho_{\text{liq}} U_{\text{eva}} \theta} = 3 \times 10^{-9} \text{ m} \left(\frac{\sigma}{0.3 \text{ N m}^{-1}} \right) \left(\frac{\rho_{\text{liq}}}{2000 \text{ kg m}^{-3}} \right)^{-1} \times \left(\frac{U_{\text{eva}}}{10^7 \text{ J kg}^{-1}} \right)^{-1} \left(\frac{\theta}{0.01} \right)^{-1}, \quad (1)$$

where n_{liq} is the number density of the liquid; U_{eva} is the latent heat of vaporization per unit mass; σ is the surface tension; $\mu = m_{\text{mol}}/N_A$ is the molecular mass (the mass of a single molecule); and θ characterizes the degree of supersaturation as

$$\theta \equiv \frac{T_{\text{sat}} - T}{T_{\text{sat}}}, \quad (2)$$

where T_{sat} is the saturation temperature.

In the kinetic nucleation theory⁴³, the rate of formation of viable nuclei I , that is, the number of condensation centres per single vapour molecule formed per unit time, is given by

$$I = \frac{n_{\text{vap}}}{n_{\text{liq}}} \left(\frac{2\sigma}{\pi \mu} \right)^{1/2} \exp \left(-\frac{U_{\text{eva}} \mu \theta}{k_B T} + \xi - \frac{4\xi^3}{27} \left(\frac{k_B T}{U_{\text{eva}} \mu \theta} \right)^2 \right), \quad (3)$$

where $\xi = \sigma \frac{4\pi r_{\text{cri}}^2}{k_B T}$. The number of clusters formed during a time interval Δt is then given as

$$N_{\text{cl}} = I \Delta t N_{\text{vap}}, \quad (4)$$

where N_{vap} is the number of vapour molecules in the cell. The surface tension σ is given as¹⁴

$$\sigma = \begin{cases} 0.3 [\text{N m}^{-1}] & \text{if } T \leq T_t \\ \sigma_0 (T_c - T)^{\frac{11}{9}} & \text{if } T > T_t, \end{cases} \quad (5)$$

where $T_c = 5,379 \text{ K}$ and $T_t = 3,500 \text{ K}$ is the transition temperature; σ_0 is continuous at T_t .

We now define $N(t, t')$ as the number of molecules in a liquid droplet at time t formed from a nucleus (formed at time t'). The degree of condensation $x_{\text{con}}(t)$ at time t —the ratio of the number of molecules in the liquid phase to the number of molecules in a given fluid (all phases)—can be given as

$$x_{\text{con}}(t) = \int_{t_1}^t I(t') N(t, t') dt', \quad (6)$$

where t_1 is the time at which the vapour reaches saturation. Note that x_{con} is the same as $x_{\text{liq}}^{\text{sup}}$ used in 'EOS thermodynamics for supersaturation'.

$N(t, t')$ is a time variable. The growth rate of $N(t, t')$ is described by the balance between the attachment of vapour molecules to the droplet surface and the evaporation from the droplet as

$$\frac{dN}{dt} = \pi r^2 n_{\text{vap}} v_{\text{th}} \left[1 - \exp \left(-\frac{U_{\text{eva}} \mu \theta}{k_B T} \right) \right], \quad (7)$$

where r is the radius of the droplet and $v_{\text{th}} = \sqrt{8k_B T / \pi \mu}$. The minimum N is that of nuclei (smallest droplets) with r_{cri} as

$$N_{\text{min}} = \frac{4}{3} \pi r_{\text{cri}}^3 n_{\text{liq}} \approx 2262 \left(\frac{r_{\text{cri}}}{3 \times 10^{-9} \text{ m}} \right)^3 \left(\frac{\rho_{\text{liq}}}{2000 \text{ kg m}^{-3}} \right), \quad (8)$$

where the number density of the liquid $n_{\text{liq}} = \rho_{\text{liq}} / \mu$ was used with an assumption of SiO_2 (that is, $m_{\text{mol}} = 60 \text{ g mol}^{-1}$).

The size evolution in a cell during a time interval Δt was solved as

$$\begin{aligned} r_{\text{min}} &= r_{\text{min}} + \left(\frac{dr}{dt} \right)_{r_{\text{min}}} \Delta t \\ r_{\text{max}} &= r_{\text{max}} + \left(\frac{dr}{dt} \right)_{r_{\text{max}}} \Delta t, \end{aligned} \quad (9)$$

where we adopted the relationship between N and r as

$$\frac{dN}{dt} = 4\pi r^2 n_{\text{liq}} \left(\frac{dr}{dt} \right), \quad (10)$$

where $N = \frac{4}{3}\pi r^3 n_{\text{liq}}$.

Here we assumed a uniform size distribution between r_{min} and r_{max} in a cell. Correspondingly, the average mass of condensate m_{ave} formed at the same specific time step (N_{cl} clusters are created at the same specific time step) is given as

$$m_{\text{ave}} \equiv \frac{\pi \rho_{\text{liq}}}{3} \frac{r_{\text{max}}^4 - r_{\text{min}}^4}{r_{\text{max}} - r_{\text{min}}}. \quad (11)$$

We allow condensation to take place at multiple time steps and track the size evolution of condensates formed at different epochs. Therefore, the final average mass and the total mass in a cell are calculated considering all the condensates formed at different times (m_{ave} and N_{cl} are tracked independently because they are formed at different times).

EOS thermodynamics for supersaturation. The ANEOS EOS is a tabular dataset with two-dimensional temperature (T) and density (ρ) grids, and each grid has corresponding internal energy (e) and pressure (P). In our hydrodynamic simulation for expanding vapour, the values of P and T for the calculating cell in the next time step are iteratively searched for from a given e and ρ via this tabular data. The default ANEOS EOS is based on the phase equilibrium, which can apply to the saturated system but cannot apply to the supersaturated system such as the rapidly expanding vapour considered in this study. We can use the default ANEOS EOS table for the single phase (gas, liquid or supercritical phase), but we need to modify the table for the gas–liquid coexistence phase to handle the supersaturated state.

In the saturated gas–liquid coexistence phase, the saturated liquid mass fraction ($x_{\text{liq}}^{\text{sat}}$) can be calculated by

$$\frac{1}{\rho^{\text{sat}}} = \frac{x_{\text{liq}}^{\text{sat}}}{\rho_{\text{liq}}^{\text{sat}}} + \frac{1 - x_{\text{liq}}^{\text{sat}}}{\rho_{\text{gas}}^{\text{sat}}}, \quad (12)$$

where ρ^{sat} , $\rho_{\text{liq}}^{\text{sat}}$ and $\rho_{\text{gas}}^{\text{sat}}$ are the total density, liquid density and gas density, respectively. The values $\rho_{\text{liq}}^{\text{sat}}$ and $\rho_{\text{gas}}^{\text{sat}}$ depend only on the temperature, and those values are given in the ANEOS EOS table. The value of $x_{\text{liq}}^{\text{sat}}$ can also be calculated from the equation of the internal energy,

$$e^{\text{sat}} = x_{\text{liq}}^{\text{sat}} e_{\text{liq}}^{\text{sat}} + (1 - x_{\text{liq}}^{\text{sat}}) e_{\text{gas}}^{\text{sat}}, \quad (13)$$

where e^{sat} , $e_{\text{liq}}^{\text{sat}}$ and $e_{\text{gas}}^{\text{sat}}$ are the total, liquid and gas internal energies, respectively. The values $e_{\text{liq}}^{\text{sat}}$ and $e_{\text{gas}}^{\text{sat}}$ depend only on the temperature, and those values are also given in the table. Equations (12) and (13) give the same value for $x_{\text{liq}}^{\text{sat}}$.

In the ‘supersaturated’ phase, similar equations can be applied,

$$\frac{1}{\rho^{\text{sup}}} = \frac{x_{\text{liq}}^{\text{sup}}}{\rho_{\text{liq}}^{\text{sup}}} + \frac{1 - x_{\text{liq}}^{\text{sup}}}{\rho_{\text{gas}}^{\text{sup}}}, \quad (14)$$

$$e^{\text{sup}} = x_{\text{liq}}^{\text{sup}} e_{\text{liq}}^{\text{sup}} + (1 - x_{\text{liq}}^{\text{sup}}) e_{\text{gas}}^{\text{sup}}, \quad (15)$$

where superscript ‘sup’ means supersaturated phase. The supersaturated liquid mass fraction ($x_{\text{liq}}^{\text{sup}}$) is calculated in the nucleation simulation and given ($x_{\text{liq}}^{\text{sup}} = x_{\text{con}}$). If we assume that liquid density does not change ($\rho_{\text{liq}}^{\text{sup}} = \rho_{\text{liq}}^{\text{sat}}$) in a given temperature between a saturated system and a supersaturated system, equation (14) gives the supersaturated gas density ($\rho_{\text{gas}}^{\text{sup}}$) for a given total density (ρ^{sup}) and a supersaturated liquid mass fraction ($x_{\text{liq}}^{\text{sup}}$). Since $x_{\text{liq}}^{\text{sup}} < x_{\text{liq}}^{\text{sat}}$, we have $\rho_{\text{gas}}^{\text{sup}} > \rho_{\text{gas}}^{\text{sat}}$. In a similar way, equation (15) gives the supersaturated gas internal energy ($e_{\text{gas}}^{\text{sup}}$) on the assumption of $e_{\text{liq}}^{\text{sup}} = e_{\text{liq}}^{\text{sat}}$.

For simplicity, here we assume that the supersaturated gas is an ideal gas. On that assumption, the internal gas energy depends only on the temperature. Therefore, $e_{\text{gas}}^{\text{sup}} = e_{\text{gas}}^{\text{sat}}$ for the same temperature. Since the value of $e_{\text{gas}}^{\text{sat}}$ is given by the default ANEOS EOS table, we can set a new value of e^{sup} for a given $x_{\text{liq}}^{\text{sup}}$, T and total density (ρ^{sup}). The supersaturated pressure (P^{sup}) can be calculated as

$$P^{\text{sup}} = \frac{1 - x_{\text{liq}}^{\text{sup}}}{\frac{\rho_{\text{gas}}^{\text{sat}}}{\rho^{\text{sup}}} - \frac{\rho_{\text{liq}}^{\text{sat}}}{\rho_{\text{liq}}^{\text{sup}}}} \times P^{\text{sat}}, \quad (16)$$

where P^{sat} is the saturated gas pressure given in the default table and depends only on the temperature. When $\rho_{\text{liq}}^{\text{sat}} \gg \rho_{\text{gas}}^{\text{sat}}$, equation (16) becomes

$$P^{\text{sup}} = (1 - x_{\text{liq}}^{\text{sup}}) \frac{\rho_{\text{gas}}^{\text{sup}}}{\rho_{\text{gas}}^{\text{sat}}} \times P^{\text{sat}}. \quad (17)$$

When the system enters the saturated gas–liquid coexistence phase, the hydrodynamic calculation with nucleation gives $x_{\text{liq}}^{\text{sup}}$, ρ^{sup} and e^{sup} . In the modified table, the temperature can be iteratively determined. Then from equations (14) and (15), $\rho_{\text{gas}}^{\text{sup}}$ and $e_{\text{gas}}^{\text{sup}}$ are calculated, respectively. The pressure can be calculated by equation (16), which is required to calculate the next time step for the vapour-expanding simulation.

So far, we have assumed the ideal gas for the supersaturated gas. However, this assumption is not valid, especially around the critical point ($T_c = 5,400$ K, $\rho_c = 550$ kg m^{−3} and $P_c = 0.19$ GPa for the SiO₂ M-ANEOS EOS). Instead of using $e_{\text{gas}}^{\text{sup}} = e_{\text{gas}}^{\text{sat}}$, we include the density dependence on $e_{\text{gas}}^{\text{sup}}$ as follows.

$$e_{\text{gas}}^{\text{sup}} = e_{\text{gas}}^{\text{sat}} + \left(\frac{\partial e}{\partial \rho} \right) (\rho^{\text{sup}} - \rho_{\text{gas}}^{\text{sat}}). \quad (18)$$

The derivative $\left(\frac{\partial e}{\partial \rho} \right)$ was calculated from the default table data in the gas-phase side near the saturated gas–liquid coexistence phase. Other than that, the procedure is the same as the case for the ideal gas assumption described in the preceding.

Settings. The initial vapour cloud was represented as a sphere with an initial radius of r_{ini} and set $r_{\text{ini}} = r_{\text{imp}}$. The initial thermodynamic conditions of the cloud were obtained from the 3D SPH impact simulations and adopted EOS as described. We assumed molar masses of $m_{\text{mol}} = 60 \times 10^{-3}$ kg mol^{−1} and $m_{\text{mol}} = 18 \times 10^{-3}$ kg mol^{−1} for SiO₂ and H₂O ice, respectively. We ignored radiative cooling because adiabatic cooling is more important (Supplementary Information).

The modelled vapour cloud was evenly spaced in the radial direction. The number of cells was 160. By testing other resolutions, we confirmed the convergence of our results. Each hemispherical cell was equally massive. Each cell was time-evolved using EOS tables (either SiO₂ ANEOS or five-phase H₂O ice EOS). We iteratively found thermodynamic variables (such as pressure P and temperature T) from the internal energy E_{int} and density ρ . The internal energy at the next time step was calculated by determining the amount of work done on or by the cell.

Electrodynamical coupling of charged nanoparticles and ions ejected from the Saturnian rings

Through the dust–plasma–magnetosphere interaction, charged nanoparticles and ions produced near Saturn’s main rings could be injected into both hemispheres of Saturn’s atmosphere^{18,20} or serve as the origin of nanometre-sized particles ejected from the Saturnian system (stream particles¹⁵). These processes contribute to the removal of exogenic impactor darkening materials from the rings following an impact on a ring particle.

Method and models. We explore the orbital evolution of charged particles under the effect of Saturn's gravitational and magnetic fields. The motion of the particle in an inertial coordinate system centred at Saturn is described by

$$\ddot{\vec{r}} = -\frac{GM_S}{|\vec{r}|^2} \hat{r} + \frac{q}{m} \left[\vec{r} - (\vec{\Omega}_S \times \vec{r}) \right] \times \vec{B}, \quad (19)$$

where G is the gravitational constant, M_S is Saturn's mass, $\vec{\Omega}_S$ is the planetary rotation frequency, \vec{B} is Saturn's magnetic field, and \vec{r} is the particle's position vector. On the right-hand side of the equation, the first term within the second bracket represents the Lorentz force, while the second term denotes the corotational electric field. The factor q/m corresponds to the electric charge-to-mass ratio and is responsible for describing the physical properties of the particle. We follow the magnetic field prescription given in ref. 18, which includes the contributions of the axisymmetric dipole, quadrupole and octopole magnetic moments (g_1^0, g_2^0 and g_3^0 , respectively). The Gauss coefficients of Saturn's magnetic field were taken from ref. 44: $g_1^0 = 21140.2$ nT, $g_2^0 = 1581.1$ nT and $g_3^0 = 2260.1$ nT. The equation of motion (equation (19)) is integrated using the ordinary differential equation integrator, developed in Python language. Our code was tested by reproducing the results of ref. 20, which include only the contribution of the magnetic dipole moment, and reproducing qualitatively and quasi-quantitatively the results of ref. 18, using a constant q/m .

We explore the orbital evolution of charged particles. Particles are excluded from the simulations when any of the following conditions is satisfied: (1) collision with Saturn, (2) location outside Saturn's Hill radius or (3) collision with the rings. The probability of collision with the rings $P_{\text{col}}(\tau)$, which is dependent on the local optical depth τ , is given as^{4,12}

$$P_{\text{col}}(\tau) = \left(1 - e^{-(\tau/\tau_s)^P}\right)^{1/P}, \quad (20)$$

where the fitting parameters are $\tau_s = 0.515$ and $P = 1.0335$. We assume that the optical depth of the rings at visual wavelengths is predominantly influenced by ring particles, given their sizes r_p are typically significantly larger than a wavelength. This can be reasonably approximated as geometric optics; $\tau \sim \int_{r_{\text{p,min}}}^{r_{\text{p,max}}} \pi r_p^2 n(r_p) dr_p$. For simplicity, we assumed $\tau = 0.01$ for $a = 66,990$ – $74,658$ (D ring), $\tau = 0.1$ for $a = 74,658$ – $92,000$ (C ring), $\tau = 2$ for $a = 92,000$ – $117,580$ (B ring), $\tau = 0.2$ for $a = 117,580$ – $122,170$ (the Cassini division), and $\tau = 1$ for $a = 122,170$ – $136,775$ (A ring). For other radial locations, we set $\tau = 0$.

Settings. The modelled charged particles are initially distributed within the ring plane, and their radial locations are uniformly distributed between $a \approx 74,658$ km and $a \approx 136,775$ km. This range spans from the inner edge of the C ring to the outer edge of the A ring, where a represents the distance from the centre of Saturn. The particles are assumed to have zero eccentricity. We employ a total of 10^5 particles, a sufficiently large number that enables us to discern the radial dependence.

The nanoparticles and ions are produced within an expanding vapour, acquiring an ejection velocity v_{ej} that matches the expansion velocity of the vapour. Consequently, the total velocity of the particles is the sum of the Keplerian velocity and the ejection velocity. The typical range of ejection velocities for an impact velocity of $v_{\text{imp}} = 30$ km s⁻¹ is approximately 0–25 km s⁻¹. Our numerical simulation is consistent with a simple analytical argument that a vapour cloud expanding into vacuum would reach the average velocity by inertia as¹³

$$\bar{v} = (2\bar{E}_0)^{1/2} \approx 14 \text{ km s}^{-1} \left(\frac{\bar{E}_0}{103 \text{ MJ kg}^{-1}} \right)^{1/2}, \quad (21)$$

where the initial specific energy of the silicate vapour $\bar{E}_0 = 103,187$ and 297 MJ kg^{-1} is obtained by our impact simulations for our $v_{\text{imp}} = 30, 40$ and 50 km s^{-1} cases, respectively.

Due to the nature of expanding hemispherical vapour, the outer part of the expanding vapour exhibits the greatest ejection velocity, while the inner region demonstrates an ejection velocity that is nearly zero¹³. We adjusted the linear distribution of ejection velocity for the simulations based on the distance to the centre¹⁴. The ejection velocity ranged from $v_{\text{ej}} = 0 \text{ km s}^{-1}$ to $v_{\text{ej}} = 25 \text{ km s}^{-1}$. This adjustment was made considering that the outer shell of the sphere has a larger volume, thus resulting in a higher probability of having a larger ejection velocity. The direction of the ejection velocity is isotropic and is limited to the leading side of the Keplerian orbit. This is because most micrometeoroid impacts occur on the leading side of a ring particle¹².

Concerning the charge-to-mass ratio value, under the assumption of a simple steady-state q/m , a particle characterized by a radius s_d and a density ρ_d is estimated to possess a charge as

$$\frac{q}{m} = \frac{3\epsilon_0\phi}{\rho_d s_d^2} \approx 1.33 \times 10^{-6} \text{ e amu}^{-1} \left(\frac{\phi}{1 \text{ V}} \right) \left(\frac{\rho_d}{2000 \text{ kg m}^{-3}} \right)^{-1} \left(\frac{s_d}{10 \text{ nm}} \right)^{-2}, \quad (22)$$

where ϵ_0 is the permittivity of the vacuum and ϕ is the surface electrostatic potential. In this study, we use a constant charge/mass ratio, denoted q/m . No explicit size distribution is assumed in this study. This is because the dependence on grain size is within the parameter q/m . The charging profiles of nanoparticles and ions play a crucial role in comprehending their behaviour. While ions possess fixed charges, the charging profile of nanoparticles and their interactions with electromagnetic forces can be easily altered due to their limited electric charge (changes in q/m are common). Consequently, stochastic charge variations can significantly influence their dynamics^{15,18}. In-depth examinations of nanoparticle and ion dynamics, in conjunction with charging processes, are required, although the primary charging mechanism has yet to be identified. In this study, we use the typical values of $\phi = 0.1$ – 1.0 V for ~ 10 nm particles obtained from a recently developed time-dependent stochastic charging method¹⁸. These values correspond to $q/m \approx 10^{-7}$ – $10^{-6} \text{ e amu}^{-1}$ (using equation (22)). We vary the charge-to-mass ratio as 1×10^{-7} , 3×10^{-7} and $1 \times 10^{-6} \text{ e amu}^{-1}$ to study the corresponding dependence.

Chemical calculations during condensation are vital for fully understanding the dynamics of ions and nanoparticles, as the impact vapour can generate various chemical species on the basis of the thermodynamic trajectory of vapour expansion and composition. Material properties, such as SiO₂ and H₂O ice, are also important since their sputtering and radiolysis reaction efficiencies differ. These investigations will be explored in future research.

Data availability

The data are available via figshare (<https://doi.org/10.6084/m9.figshare.27288567>).

Code availability

Codes for the SPH, condensation and dynamical simulations may be provided upon request.

References

- Monaghan, J. J. Smoothed particle hydrodynamics. *Annu. Rev. Astron. Astrophys.* **30**, 543–574 (1992).
- Monaghan, J. J. On the problem of penetration in particle methods. *J. Comput. Phys.* **82**, 1–15 (1989).
- Monaghan, J. J. & Lattanzio, J. C. A refined particle method for astrophysical problems. *Astron. Astrophys.* **149**, 135–143 (1985).
- Genda, H., Fujita, T., Kobayashi, H., Tanaka, H. & Abe, Y. Resolution dependence of disruptive collisions between planetesimals in the gravity regime. *Icarus* **262**, 58–66 (2015).

34. Kurosawa, K. et al. Assessment of the probability of microbial contamination for sample return from Martian moons II: the fate of microbes on Martian moons. *Life Sci. Space Res.* **23**, 221–45532 (2019).
35. Okamoto, T., Kurosawa, K., Genda, H. & Matsui, T. Impact ejecta near the impact point observed using ultra-high-speed imaging and SPH simulations and a comparison of the two methods. *J. Geophys. Res. Planets* **125**, e2019JE005943 (2020).
36. Canup, R. M., Barr, A. C. & Crawford, D. A. Lunar-forming impacts: high-resolution SPH and AMR-CTH simulations. *Icarus* **222**, 200–219 (2013).
37. Kraus, R. G., Senft, L. E. & Stewart, S. T. Impacts onto H₂O ice: scaling laws for melting, vaporization, excavation, and final crater size. *Icarus* **214**, 724–738 (2011).
38. Pierazzo, E. & Chyba, C. F. Cometary delivery of biogenic elements to Europa. *Icarus* **157**, 120–127 (2002).
39. Pruß, A., and Wagner, W. in *Physical Chemistry of Aqueous Systems: Meeting the Needs of Industry* (eds White, H. J. Jr et al.) 66–77 (ACS, 1995).
40. Morishima, R. & Edgington, S. G. Regolith grain sizes of Saturn's rings inferred from Cassini-CIRS far-infrared spectra. *Icarus* **221**, 888–899 (2012).
41. Okamoto, T. et al. Impact experiments of exotic dust grain capture by highly porous primitive bodies. *Icarus* **224**, 209–217 (2013).
42. O'Keefe, J. D. and Ahrens, T. J. in *Geological Implications of Impacts of Large Asteroids and Comets on the Earth* (eds Silver, L. T. & Schultz, P. H.) 103–109 (GSA, 1982).
43. Girshick, S. L. & Chiu, C. P. Kinetic nucleation theory: a new expression for the rate of homogeneous nucleation from an ideal supersaturated vapor. *J. Chem. Phys.* **93**, 1273–1277 (1990).
44. Dougherty, M. K. et al. Saturn's magnetic field revealed by the Cassini Grand Finale. *Science* **362**, aat5434 (2018).

Acknowledgements

R.H. acknowledges the financial support of JSPS Grants-in-Aid (JP17J01269, 18K13600, 23KK0253). H.G. acknowledges the financial

support of JSPS Grants-in-Aid (21H04514, 20KK0080, 22K21344). G.M. thanks the Institut de Physique du Globe de Paris and European Research Council, France (101001282, METAL). The dynamic simulations of charged particles were performed on the S-CAPAD/DANTE platform, IPGP, France. We deeply thank S. Charnoz and A. Crida for discussion. We thank B.C. Johnson for the discussion on the EOSs, Z. Zhang for the discussion on the detectable darkening properties by the Cassini's Radiometry observations, J. O'Donoghue for the discussion on the ring rain and R. Morishima for the discussion on the size distribution of the ring particles.

Author contributions

R.H. designed the study, wrote the paper, performed the simulations, analysed the results and prepared the figures. H.G. developed SPH code for impact simulations and made EOS for supersaturation. G.M. performed dynamical simulations of charged particles.

Competing interests

The authors declare no competing interests.

Additional information

Supplementary information The online version contains supplementary material available at <https://doi.org/10.1038/s41561-024-01598-9>.

Correspondence and requests for materials should be addressed to Ryuki Hyodo.

Peer review information *Nature Geoscience* thanks Hsiang-Wen Hsu, Valery Lainey and the other, anonymous, reviewer(s) for their contribution to the peer review of this work. Primary Handling Editor: Tamara Goldin, in collaboration with the *Nature Geoscience* team.

Reprints and permissions information is available at www.nature.com/reprints.